

A New Synergistic Approach for Monitoring Wetlands Using Sentinels -1 and 2 data With Object-based Machine Learning Algorithms

Andrew Whyte¹, Konstantinos P. Ferentinos², George P. Petropoulos^{1, 3, *}

¹Department of Geography and Earth Sciences, University of Aberystwyth, SY23 2DB, Wales, UK.; petropoulos.george@gmail.com; george.petropoulos@aber.ac.uk

²Department of Agricultural Engineering, Institute of Soil & Water Resources, Hellenic Agricultural Organization "Demeter", 61 Dimokratias Av., 13561, Athens, Greece; kpf3@cornell.edu

³Department of Mineral Resources Engineering, Technical University of Crete, Chania, Greece;

*Correspondence: petropoulos.george@gmail.com; Tel: +44-01970 621861

Abstract

In this work the synergistic use of Sentinel-1 and 2 combined with the System for Automated Geoscientific Analyses (SAGA) Wetness Index in the content of land use/cover (LULC) mapping with emphasis in wetlands is evaluated. A further objective has been to a new Object-based Image Analysis (OBIA) approach for mapping wetland areas using Sentinel-1 and 2 data, where the latter is also tested against two popular machine learning algorithms (Support Vector Machines - SVMs and Random Forests - RFs). The highly vulnerable iSimangaliso Wetland Park was used as the study site. Results showed that two-part image segmentation could efficiently create object features across the study area. For both classification algorithms, an increase in overall accuracy was observed when the full synergistic combination of available datasets. A statistically significant difference in classification accuracy at all levels between SVMs and RFs was also reported, with the latter being up to 2.4% higher. SAGA wetness index showed promising ability to distinguish wetland environments, and in combination with Sentinel-1 and 2 synergies can successfully produce a land use and land cover classification in a location where both wetland and non-wetland classes exist.

Keywords: *Support Vector Machines, Random Forests, object-based classification, Sentinel-1, Sentinel-2*

1. Introduction

Wetland systems are precious natural environments of a thriving flora and fauna biota, multifaceted hydrological network and critical biogeochemical cycles. They are highly effective at preventing flooding (Loveline, 2015), protect coastlines from breaching tidal waters (Gedan et al., 2010), act as carbon sinks whilst being large suppliers of oxygen (Kayranli et al., 2009), provide fertile farming lands (Rippon, 2009) and have intrinsic qualities which can help the human mind (Gesler, 2005). Despite their importance, many wetlands around the globe are under threat due to natural and anthropogenic climate change, as well as, changes in land use brought about by increasing populations and urban expansion. Over the last century, it has been estimated that

44 50% of the world's wetlands have disappeared, with an increased rate of 3.7 times that during the
45 20th and 21st centuries (Davidson, 2014). Therefore, it is becoming increasingly important to
46 study and monitor wetlands due to their sensitivity to external and internal changes, as these can
47 initiate the detrimental process of wetland degradation, thus, depleting the biodiversity and
48 affecting the livelihood of many people around the globe that rely on them.

49 Remote sensing and Geographical Information Systems (GIS) technologies provide a valuable tool
50 when monitoring the Earth's surface. Satellite imagery can capture specific moments in time that
51 can be analyzed and processed to offer an extensive range of products to be used in a vast array of
52 applications. Remote sensing also provides the ability to monitor large regions of land which may
53 be inaccessible for *in situ* strategies (Gauci et al., 2018; Aune-Lundberg, Linda et al., 2014). Land
54 use and land cover (LULC) mapping is one such application, allowing for short or long-term
55 change detection and monitoring in vulnerable habitats (Xu et al., 2017). It also allows for
56 effective evaluation of any management practices that are introduced, which is in great need in
57 protected conservation areas (Bassa et al., 2016). This ability to study changes in the environment
58 with earth observation data, presents decision makers with critical visual and statistical
59 information that can be used to mitigate or adapt before a threshold is crossed, after which the
60 chances of landscape regeneration may become too high.

61 Vast quantities of data are being produced by satellites with numerous sensors launched just in
62 the last decade. The introduction of the Sentinel satellite systems by the European Space Agency
63 (ESA) is contributing to this whilst carrying on the long-term continuity missions of past and
64 present satellites, offering relatively high spatial, temporal and spectral resolution imagery and
65 doing so with a variety of sensor types (optical, radar and thermal) (Berger et al., 2012). The key
66 purpose of the Sentinel Mission is to support policy making for the Global Monitoring for
67 Environmental Security (GMES) program, while providing new opportunities for the scientific
68 community (Aschbacher and Milagro-Pérez, 2012). The Sentinel satellites can play a pivotal role
69 in future land surface monitoring programs, especially if the synergistic collaboration between
70 them is explored, therefore this has to be a key area to develop (Malenovský et al., 2012).

71 The application of classification algorithms in remote sensing is often based on per-pixel
72 classifiers (Wang, 2012; Xu et al., 2017; Murray-Rust et al., 2014). Those techniques are based on
73 assigning individual image pixels with a user-defined class based on the spectral characteristics of
74 the individual pixels, either identified computationally, with minimum user input (unsupervised),
75 or through user-defined training pixels (supervised). Although pixel-based classifications have
76 been successfully used in wetland classifications, many researchers believe that object-based
77 image analysis (OBIA) can provide more accurate classification results. Dronova (2015), in a
78 review of 73 studies reported that OBIA improves wetland classifications by 31% compared to
79 pixel-based methods. Mui et al. (2015) underlined that although OBIA is a promising concept,
80 further research is needed to test it in a range of environments, with a variety of sensors. There
81 have been many remote sensing studies that have implemented OBIA for mapping land cover.
82 These include glacier delineation and debris cover (Ardelean et al., 2011; Rastner et al., 2014;
83 Robson et al., 2015), urban infrastructure (d'Oleire-Oltmanns et al., 2011), agriculture (Forster et
84 al., 2010; Taşdemir et al., 2012), and forestry mapping (Dorren et al., 2003; Guo et al., 2012;
85 Lindquist and D'Annunzio, 2016), to name but a few. The application of OBIA in wetland mapping
86 has not been to the same extent as the disciplines mentioned above in the literature, but it has
87 seen a growth in the last decade with new advances coming through (Harken and Sugumaran,
88 2005; Mas et al., 2014).

89 Machine learning algorithms have become an integral part of remote sensing studies in recent
90 years due to their durability and capability in performing LULC classifications (Rogan et al., 2008;
91 Xu et al., 2017; Gauci et al., 2018). Amongst them, the most popular algorithms are Random
92 Forests (RFs) (Breiman, 2001) and Support Vector Machines (SVMs) (Cortes and Vapnik, 1995).
93 Several studies have demonstrated so far that those algorithms consistently outperform many
94 other frequently used classifiers (Shang and Chisholm, 2014), making them suitable for many
95 scenarios over a range of disciplines. These machine learning algorithms are powerful techniques
96 with a great deal of flexibility, thus, allowing them to be implemented on a variety of sensor types
97 and combinations. The use of such classifiers offers promising proficiency in avoiding challenges
98 associated with heterogeneous environments and limited training sample ability, which is often a
99 problem in wetlands, where high resolution imagery and *in situ* measurements may be expensive
100 or difficult to collect. There have been several successful applications of both SVMs (Petropoulos
101 et al., 2012; Petropoulos et al., 2013; Scott et al., 2014; Sonobe et al., 2014; Szantoi et al., 2013;
102 Zhang and Xie, 2013) and RFs (Furtado et al., 2016; Maxwell et al., 2016; Mellor et al., 2013;
103 Sesnie et al., 2010) in remote sensing. Niculescu et al. (2017) conducted a study with RFs, and a
104 synergistic classification using Sentinel-1 and 2 for a coastal wetland in Romania. This study used
105 a pixel based approach and found a synergistic technique provided the highest accuracy. Dronova
106 (2015) called for more studies to be focused on the application of OBIA and machine learning
107 algorithms, with comparisons needed between different algorithms. To our knowledge, the use of
108 these advanced image processing algorithms with OBIA, combined with data from sophisticated
109 satellites launched recently such as Sentinel-1 and 2, has not yet been adequately investigated.

110 The aim of this study is to develop a synergistic approach between Sentinel-1 and 2 in the context
111 of wetland mapping. In particular, it aims at analyzing a number of secondarily derived products
112 from the sensors mentioned above, along with the topographically derived SAGA Wetness Index
113 (SWI), to evaluate their ability to map a complex area containing wetland and non-wetland LULC
114 classes. A further objective has been to a new Object-based Image Analysis (OBIA) approach for
115 mapping wetland areas using Sentinel-1 and 2 data, where the latter is also tested against two
116 popular machine learning algorithms (SVMs and RFs).

117

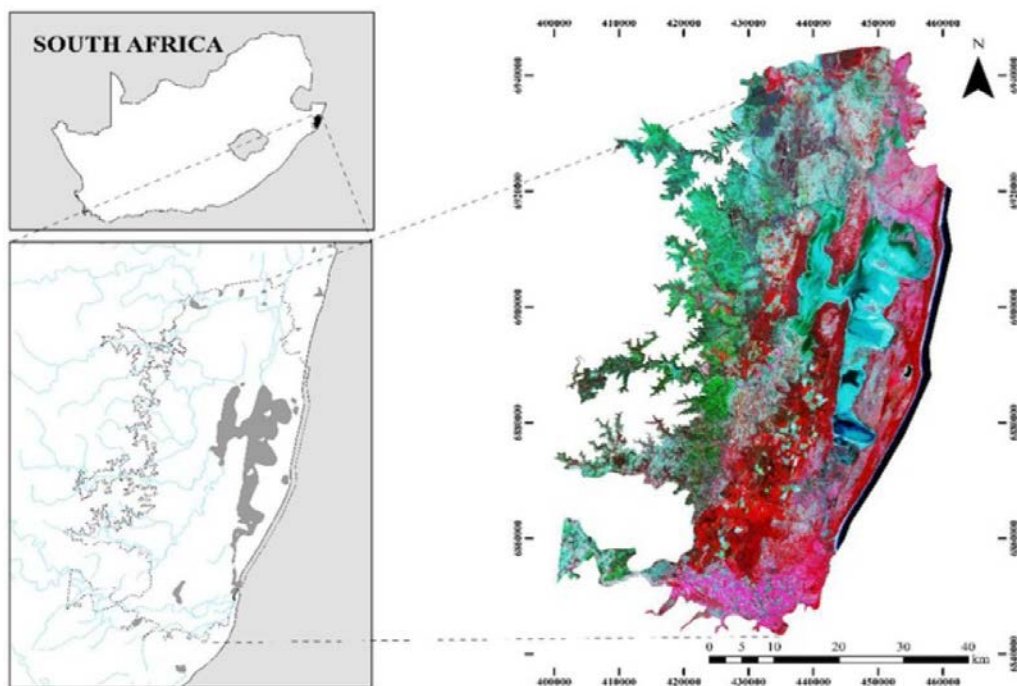
118 **2. Materials and Methods**

119 *2.1. Study site*

120 The study site under consideration is the iSimangaliso Wetland Park, also known as the Greater
121 St. Lucia Wetland Park, located on the east coast of South Africa in the northern stretch of
122 KwaZulu-Natal Province. It lies between the longitudes 32°21'E, 32°34'E, and latitudes 24°34'S,
123 28°24'S, covering a land surface area of 3280 km², making it the largest estuarine system in South
124 Africa and one of the largest in the world (Figure 1). The east coast consists of a succession of
125 raised sand dunes and indignant woodland; that help protect the wetland from tidal surges and
126 strong winds. The climate is considered to be sub-tropical with mean annual temperatures
127 greater than 21°C. The park's rainfall varies both temporally and spatially, due to a combination of
128 elevation change (~170 m from the western hills to the coastal wetland), climate zone and sea-
129 land dynamics. Annual precipitation can range from 1200 and 1300 mm (Bassa et al., 2016),
130 however below normal precipitation has been recorded in 2015 (Coppola, 2015) and early 2016,
131 due to drought. The wetland is fed by five contributing catchments and rivers.

132 The park hosts a variety of wetland vegetation types, making it a highly diverse, heterogeneous
133 environment to study. Much of the vegetation colonized the area in its recent history due to falling

134 lake levels, with depths rarely exceeding 1.5 m (Whitfield and Taylor, 2009). The wetland
135 vegetation consists of salt marsh species that thrive in brackish systems, such as the salt marsh
136 rush (*Juncus kraussii*) and tasselweed (*Ruppia martima*); saline reed swamps, often found at
137 estuarine edges with species such as reed grass (*Phragmites mauritianus*) (Macnae, 1963); sedge
138 swamps, containing *Eleocharis limosa*; floodplain grasses, predominantly Antelope Grass
139 (*Echinochloa pyramidalis*); furthermore, the most dominant wetland vegetation type in the park
140 are from river fed freshwater swamps that host a variety of species (Adam et al., 2009). Since the
141 closure of the St. Lucia mouth to the Indian Ocean in 2002, the once thriving mangrove
142 communities (Macnae, 1963), have fallen dramatically, due to the drop in salinity levels. Adam et
143 al. (2013) explain how this has made way for reed species, whose numbers have risen. The two
144 most notable freshwater swamps in the park are the Mkhuze Swamp located north of the
145 Northern Lake and the Mfolozi Swamp located to the far south of the estuarine system adjacent to
146 the Mfolozi River floodplain. Both swamps are under pressure from illegal farming practices that
147 are encroaching on them.



148
149 **Figure 1.** Study site map of the iSimangaliso Wetland Park, South Africa. False color image clearly
150 defines key features of the landscape.

151 2.2. Data sets

152 Single Look Complex (SLC) Sentinel-1 (C-band at 5.405 GHz) imagery was acquired from the
153 European Space Agency Sentinel Data Hub, for the 30th June 2016 in Interferometric Wide Swath
154 Mode (IW). This produces a 250 km swath at approximately 5x20 m resolution. The imagery was
155 captured on ascending path in dual-polarization mode at VV+VH, as this was the only option
156 available for the region. The study area was contained in the IW Beam 2 giving an incidence angle
157 of 36.47°-41.85° and 34.77°-40.15° for the minimum and maximum orbit altitudes, respectively.

158 The Sentinel-2 optical imagery was also acquired from the European Space Agency Sentinel Data
159 Hub for the 30th June 2016 with the multispectral imager (MSI) instrument at 7:49 am. This was
160 the only day where imagery from both Sentinel-1 and 2 matched, offering a prime opportunity for
161 a synergistic study. Cloud cover was at 0%, allowing for all features to be classified without the
162 need for cloud masking. The instrument offers 13 spectral bands ranging from 443 nm to 2190

163 nm. The highest resolutions are captured in the three visible and one NIR band (10 m), followed
 164 by six red edge/SWIR bands (20 m) and three coarse atmospheric correction bands (60 m). For
 165 this study, only the spectral information acquired in the four 10 m and one 20 m SWIR (1610 nm)
 166 bands was utilized.

167 The final dataset which was acquired was the Shuttle Radar Topography Mission's (SRTM) 1 arc-
 168 second Digital Elevation Model. This was downloaded from USGS Earth Explorer and offers a void
 169 filled elevation model with a resolution of 30 meters, created with interferometry using C-band
 170 radar. A summary of the datasets used in this study can be found in Table 1.

171 **Table 1.** Summary of the remotely sensed datasets used for this study.

Sensor Name	Sensor type	Acquisition Date	Band Information	Resolution (m)
Sentinel-2	Optical	30/06/20 16	Blue (490nm)	10
			Green (560nm)	10
			Red (665nm)	10
			NIR (842nm)	10
			SWIR (1610nm)	20
Sentinel-1	C-Band Radar	30/06/20 16	VV + VH	5x20
SRTM	C-Band Radar	2000	DEM	30

172

173 2.3. Pre-processing and secondary derivatives

174 All radar imagery acquired was pre-processed using the Sentinel Application Platform (SNAP)
 175 which offers a range of tools and features suitable for Sentinel-1 imagery processing and analysis.
 176 Due to the large swath width, the image was first subset to the study site extent, helping increase
 177 processing time. The remaining sub-swaths were then merged using TOPSAR de-bursting and the
 178 precise orbit file was fused to offer the highest geometric precision. Polarimetric speckle filtering
 179 was performed using the Refined Lee Filter (Lee, 1981) with a window size of 7x7, as suggested
 180 by Shitole et al. (2015).

181 The next step taken was to perform radiometric calibration to convert the pixel's digital number
 182 (DN) into sigma0 (σ^0) backscatter values which directly relate to actual scene backscatter. This
 183 was achieved using the following equation:

$$184 \quad \sigma^0 = \frac{|DN_i|^2}{A_i^2} \quad (1)$$

185 This step was performed on VV and VH, where A_i is an absolute calibration constant found in the
 186 products Look Up Table (LUT). A complex output file was also created for further analysis.

187 For the purpose of this study the full capabilities of the Sentinel-1 dual-polarized imagery was
 188 tested in order to get a good understanding of its effectiveness in LULC mapping. Therefore, the
 189 Cloude and Pottier (1997) H-Alpha ($H-\alpha$) decomposition was included, allowing for entropy and
 190 alpha derivatives to be extracted from the data. To calculate a dual- polarized $H-\alpha$ decomposition,
 191 a 2x2 coherency matrix (T_{dual}) was created using the complex data for every image pixel. This is
 192 an adaptation from the 3x3 coherency matrix that is commonly applied to quad-polarized data

193 (Xie et al., 2015), and was first proposed by Cloude (2007). It was calculated and implemented in
 194 SNAP using the following equation:

$$195 \quad T_{dual} = \begin{pmatrix} T_{11} & T_{12} \\ T_{12} & T_{22} \end{pmatrix} = U \begin{bmatrix} \lambda_1 & \\ & \lambda_2 \end{bmatrix} U^H = \lambda_1 u_1 u_1^H + \lambda_2 u_2 u_2^H \quad (2)$$

196 thus, a single complex covariance matrix (T_{dual}) can be expanded into a weighted sum of two
 197 simpler matrices, allowing for the pseudo-probabilities (P_i) to be defined using the sorted
 198 eigenvalues (λ). Given the eigenvectors and probabilities, entropy (H) and alpha (α) values can be
 199 derived per pixel, as shown in the following equations:

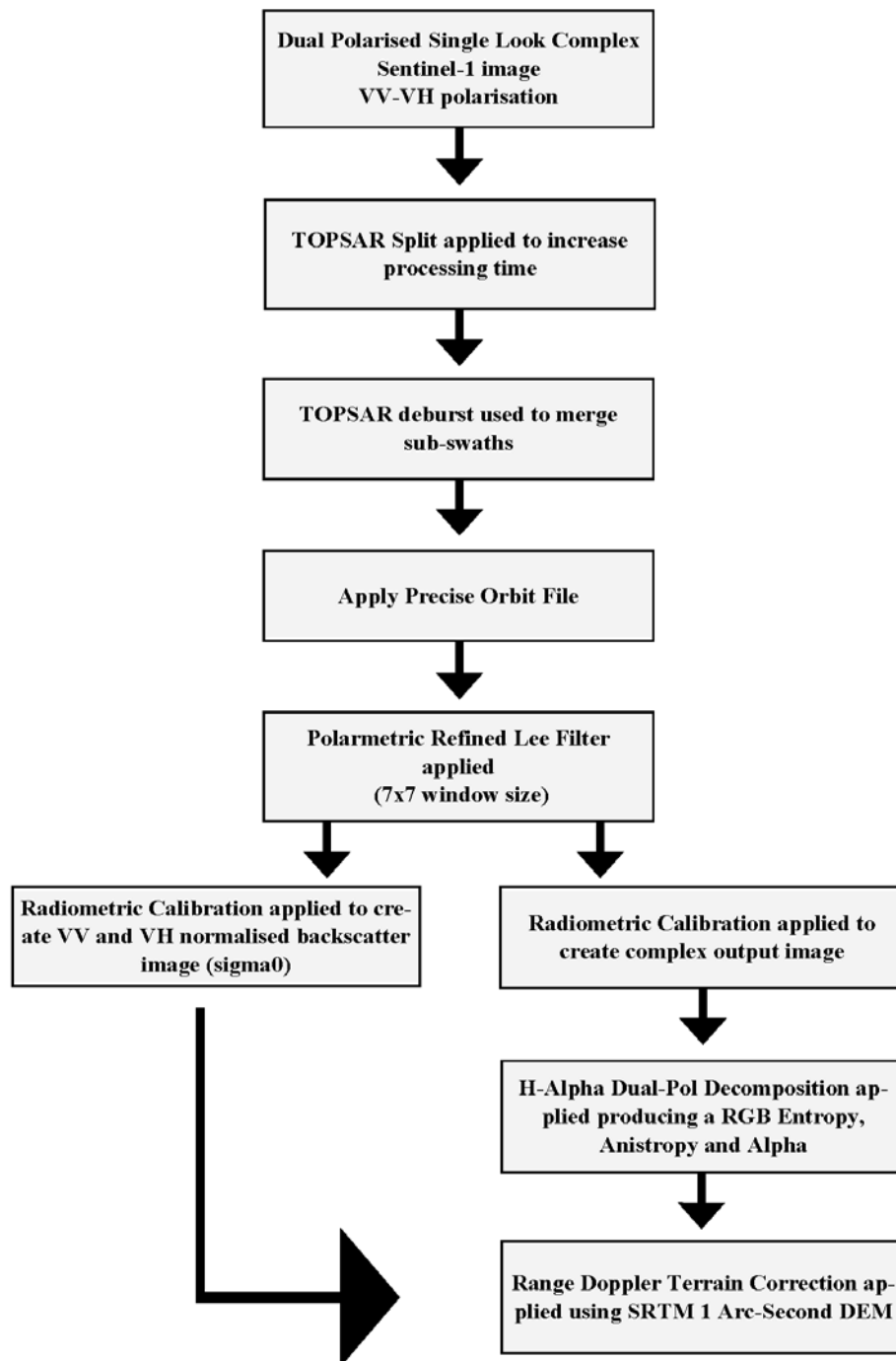
$$200 \quad H = \sum_{i=1}^2 -P_i \log_2 P_i \quad \text{and} \quad \alpha = \sum_{i=1}^2 P_i \cos^{-1}(|u_{1i}|) \quad (3)$$

201 where,

$$202 \quad P_i = \lambda_i / \sum_{j=1}^2 \lambda_j, \quad i = 1, 2 \quad (4)$$

203 The σ^0 and $H-\alpha$ outputs were terrain corrected using SNAP's 'Range Doppler Terrain Correction'
 204 algorithm with a SRTM 1 Arc-Second DEM. Terrain correction helps improve the geometric
 205 representation of the real-world surface. This is needed because during image capture,
 206 topographical variations and off-nadir distortion unsettles the image (Wang et al., 2013). A
 207 bilinear interpolation resampling method was used for the correction. Once all pre-processing
 208 was completed in SNAP the images were exported as GeoTIFF files, projected to WGS-84 UTM
 209 Zone 36S and resampled to 10 m resolution to match that of the optical imagery. Figure 2 shows
 210 the processing steps taken in STEP in chronological order.

211 Atmospheric correction of the optical imagery was conducted in QGIS using the Semi-Automatic
 212 Classification Plugin, which applies a dark object subtraction algorithm, converting the top of
 213 atmosphere values into surface reflectance values. The two Sentinel-2 scenes were joined in
 214 ArcMap 10.3 using the 'Mosaic to New Raster' tool, then georeferenced and projected to WGS-84
 215 UTM Zone 36S. Bands 2 (Blue), 3 (Green), 4 (Red), 8 (NIR) and 11 (SWIR) were isolated for this
 216 study, and SWIR was resampled to 10 m spatial resolution, matching that of the other four bands.



217

218 **Figure 2.** Flow diagram of the SAR pre-processing stages that was implemented in SNAP. The
 219 flow splits due to the creation of two SAR derivatives ($H-\alpha$ and σ_0).

220

221 The commonly used Normalized Difference Vegetation Index (NDVI) was used to help
 222 discriminate vegetation types, for both non-wetlands and wetlands. NDVI also helps distinguish
 223 between vegetation and non-vegetation classes within the image. Another common index used in
 224 remote sensing studies is the Normalized Difference Water Index (NDWI) (McFeeters, 1996). This
 225 index looks at the difference between the green and near infrared bands, as they are strongly
 226 absorbed by water bodies making delineation easier. However, NDWI is sensitive to built-up land,
 227 resulting in over-estimation (Du et al., 2016). Here, the advantage of the SWIR band is taken by

228 implementing the Modified Normalized Difference Index (MNDWI), proposed by Xu (2006), who
229 noted the much stronger absorption of SWIR by open water.

230 The Shuttle Radar Topography Mission (SRTM) tiles were joined in ArcMap 10.3 using the '*Mosaic
231 to New Raster*' tool before being bi-linearly resampled to 10 m resolution. An important aspect
232 was the introduction of a wetness index to the classification, to try to help distinguish LULC
233 classes in wetlands and neighboring non-wetlands. The freely available SAGA Wetness Index
234 (SWI) was chosen over the more commonly used Topographic Wetness Index (TWI). This index,
235 although similar, uses a modified catchment area calculation, aimed to model flow as a more
236 realistic process, instead of thin, unrealistic flow paths. TWI uses a single-direction based flow
237 algorithm (D8), whereas SWI utilizes a multi-directional flow algorithm (MD8). The SAGA
238 Wetness Index should allow for a more accurate wetland delineation in the classification stages
239 (Andersson, 2009).

240 Finally, image stacking was a key step in the processing chain, because it makes the classification
241 stage more computationally efficient (Arenas and Pradenas, 2016). Stacking of the images was
242 conducted in ArcMap 10.3 using the '*Composite Bands*' tool with the VV σ^0 , Entropy, Alpha, Blue,
243 Green, Red, NIR, NDVI, MNDWI and SWI bands. The VH σ^0 backscatter image was discarded after
244 stretching and visual inspection due to low image contrast around water bodies, mudflats and
245 agricultural areas. After the stacked image had been produced, the image was clipped to the study
246 site extent. The clipping was done at this stage to ensure that all bands were of equal dimensions.

247

248 *2.4. Image classification and accuracy assessment*

249 Image segmentation and classification were implemented in eCognition 9.0. This technique has
250 been used in many wetland OBIA studies with promising results (Dronova, 2015; Dronova et al.,
251 2011; Frohn et al., 2011; Jung et al., 2015). A two-stage image segmentation was carefully chosen,
252 followed by object sample selection and classification, using SVMs and RFs for three combinations
253 of data, consisting of *Op*, *OpR* and *OpRS*. More specifically, for image segmentation, only the Blue,
254 Green, Red, NIR and NDVI optical bands were used, because none of them was subject to
255 resampling, as they were all captured at 10 m spatial resolution. Thus, edge features were well
256 preserved compared to the bands. The radar imagery did not offer enough detail for
257 segmentation, due to their resolution, image noise and lower feature distinguishability. The image
258 was stretched using a standard deviation of 2.5 prior to segmentation. Band weighting was kept
259 at 1, with the exception of the NIR and NDVI bands that were assigned double. This forces the
260 segmentation to be influenced more by these bands, as it was found that better delineation of
261 agricultural fields and sparse vegetation could be achieved, possibly due to greater band contrast.
262 The multi-resolution segmentation algorithm was implemented on the stacked image to group
263 pixels based on the homogeneity. Additionally, a secondary stage of segmentation was included,
264 due to the high heterogeneous wetland study site, as suggested by Grenier et al. (2008). The
265 spectral difference algorithm was used in conjunction with the multiresolution segmentation to
266 merge objects further based on a user-defined threshold. Parameter weightings were chosen
267 through trial and error with a scene subset that represented a satisfactory heterogeneous sample.
268 It was found that a low shape to high color ratio produced the best results, with the total number
269 of objects being 6740.

270 In eCognition, the user can state what features are to be created when the segmentation is
271 initiated. For this study, the mean value of all the composite image bands constrained by the
272 object was calculated (spectral features), as well as the objects shape index, roundness and

273 rectangular fit (geometric features). In situ ground truth data was not available, so a WorldView-1
 274 panchromatic satellite image was acquired for the 29th June 2016 (1-day difference to Sentinel-1
 275 and 2). This provided 0.46 m resolution imagery in with good feature distinguishability to help
 276 with training and validation. A downside was that the imagery did not cover the full extent of the
 277 study site. Therefore, full-color Google Earth imagery was also used with a 2-month acquisition
 278 difference to compliment the WorldView-1 data. Out of the total 6740 objects, 10% (674) were
 279 chosen for training to classify the LULC classes. Fifteen classes were chosen, based on previous
 280 studies for this region and the standard South African classification scheme proposed by
 281 Thompson (1996). Table 2 shows the classes and descriptions used, which includes both wetland
 282 and non-wetland classes. Each class was therefore trained with 45 samples that were carefully
 283 chosen using the WorldView-1 and Google Earth images. It was ensured that, where possible,
 284 sample objects were taken from across the entire scene to stop bias in the SWI band.

285

286 **Table 2.** LULC classification scheme with the class code used for graphs and a brief class
 287 description.

LULC Classes	Class Code	Class Description
Agriculture (High Productivity)	1	Non-wetland class where healthy, high yield arable farming is present.
Agriculture (Low Productivity)	2	Non-wetland class with low yields or emergent crops often present after the field is ploughed.
Agricultural Wetland (High Productivity)	3	Irrigated, healthy and high yield farming practices that occur on organic soils on the wetland (sugar cane).
Agricultural Wetland (Low Productivity)	4	Irrigated, low yield or emergent crops that occur on organic soils on the wetland (sugar cane).
Aquatic Macrophyte	5	Aquatic plants that is either emergent, submerging or floating in water.
Dry Mudflat	6	Exposed lake, river or estuarine bed that has been allowed to dry out.
Grassland	7	Non-wetland class where long or short grass species dominate with sparse trees and bushes if any.
High Vegetated Wetland	8	Highly vegetated area consisting of larger vegetation species (e.g. swamps and mangroves).
Low Vegetated Wetland	9	Sparsely vegetated area with short grasses and small wetland plant species.
Open Water	10	Exposed fresh or saline surface water.
Sand/Soil	11	Bare land or beaches/dunes, with very low or no vegetation cover.
Thicket/Dense Bush	12	Non-wetland class with a thick or dense packing of shrubs, bushes and small trees with pockets of grassland.
Urban	13	Areas dominated by artificial surfaces and features, such as, roads, houses or small holdings.
Wet Mudflat	14	Recently exposed lake, river or estuarine bed that has not had time to dry out fully and crack.
Woodland	15	Non-wetland class with a large presence of indigenous trees ranging from medium to large sizes.

288

289 Before the classification was applied to the whole dataset, the optimum parameters of the SVMs
 290 were established. The RBF kernel was used due to its robustness and promising capabilities over
 291 linear and polynomial kernels (Kavzoglu and Colkesen, 2009; Paneque-Gálvez et al., 2013), which
 292 consists of the C and γ parameters. The optimum values were found by performing an overall
 293 accuracy assessment of the objects contained within the subset used for the segmentation
 294 parameters. For our dataset, we found a C value of 2000 and γ value of 0.06 worked best.

295 Similarly, the same parameter selection approach was taken for RFs. An optimum value of 900
 296 was found for the number of trees, and a value of 14 for the number of variables to be tested at
 297 each node. After parameter selection, the entire scene was classified with the three combinations
 298 of datasets. That is, optical only (*Op*), optical and radar only (*OpR*) and optical, radar and SWI
 299 (*OpRS*). All bands were normalized prior to running the classification. Each classification image
 300 was then exported in shapefile format with class names and object information, ready to be
 301 validated, analyzed and made into a map using ArcMap 10.3.

302 An accuracy assessment was carried out on all six classification images using an error matrix to
 303 help evaluate the classifier algorithms and product synergies. The technique has been used in
 304 countless studies and has the benefit of revealing commission and omission errors in the data
 305 (Congalton, 1991). Each classifier was evaluated using producer accuracies, user accuracies,
 306 overall accuracy and the Kappa coefficient; with an overall sample size of 1650 pixels, equating to
 307 ~110 samples per class. Producer's accuracy (1- error of omission) is a measurement of the
 308 percentage of correctly classified pixels or objects per class. User's accuracy measures the
 309 percentage of correctly mapped pixels or objects per class. Kappa is used as an indicator of
 310 agreement between the classified image and ground truth data, showing whether the values of an
 311 error matrix are statistically better than random (Foody, 2004; Murayama, 2012), and is given by
 312 the following equation:

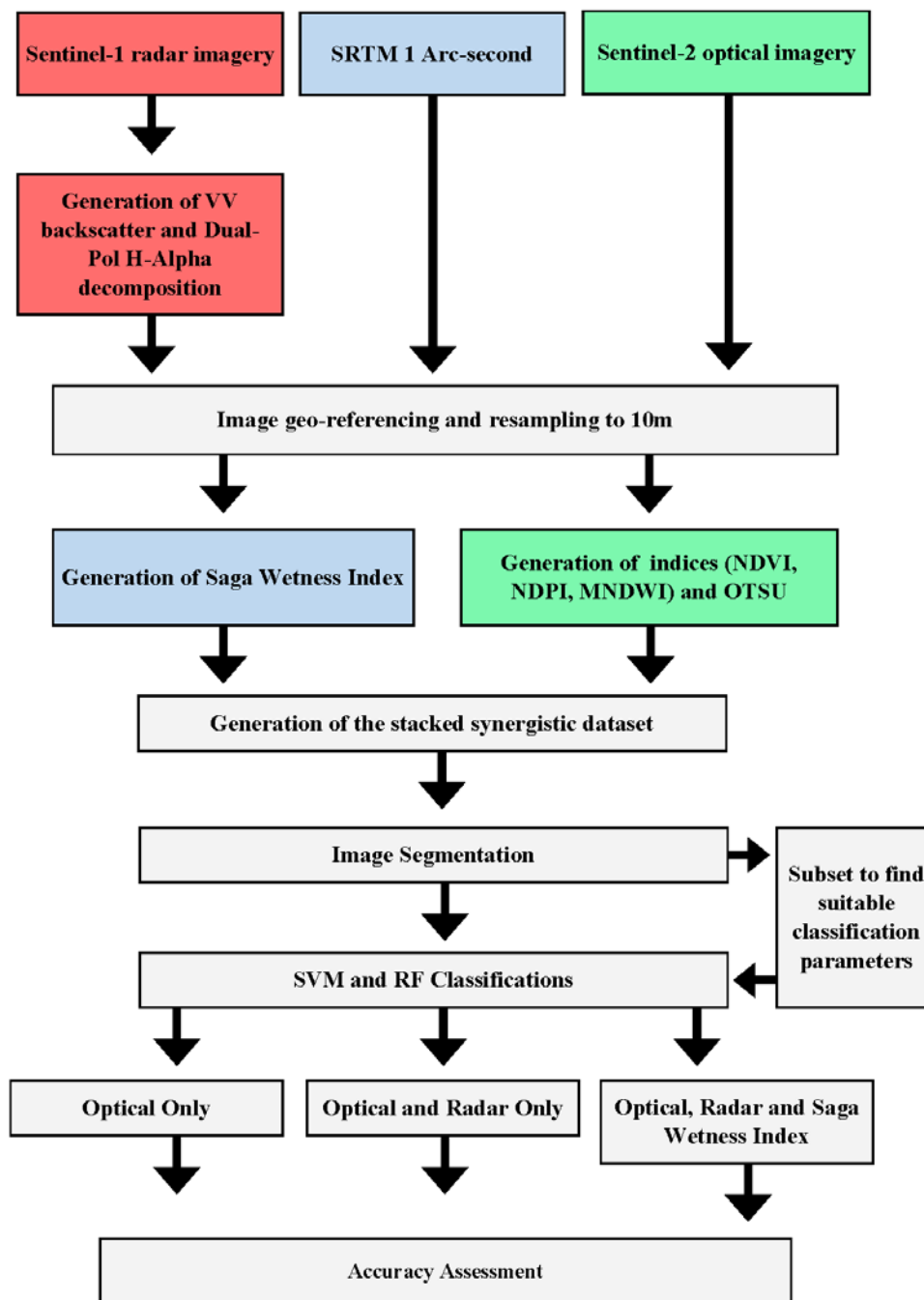
$$313 \quad Kappa = \frac{n \sum_{i=1}^q n_{ii} - \sum_{i=1}^q n_{Ri} n_{Ci}}{n^2 - \sum_{i=1}^q n_{Ri} n_{Ci}} \cdot 100 \quad (5)$$

314 where, q is the number of classes, n_{ii} are the diagonal elements of the confusion matrix, n is the
 315 total number of sampled objects, n_{Ci} represents the marginal sum of the columns, and n_{Ri} is the
 316 marginal sum of the rows. Landis and Koch (1977) suggested guideline values be followed when
 317 evaluating classifiers using Kappa for categorical data; where values greater than 0.81 are
 318 considered as almost perfect agreement, 0.61 to 0.80 indicate substantial agreement, 0.41 to 0.60
 319 suggest moderate agreement, 0.21 to 0.40 indicates poor agreement and values below 0.20 have
 320 no agreement whatsoever. The accuracy assessment was conducted in ArcMap 10.3 using a
 321 combination of WorldView-1 and Goggle Earth images.

322 The Kappa values can be compared using a Z-Test to study any significance between them.
 323 However, the test assumes that the samples are independent for each classifier. When a
 324 dependent sample set is available, the McNemars's test can be used to compare two or more
 325 samples (de Leeuw et al., 2006). The test is non-parametric based on a binary 2x2 contingency
 326 matrix, closely related to the chi-squared statistic which can be adapted to compare multiple
 327 classifiers. The sample set is labelled with f_{12} and f_{21} which are the number of correct samples for
 328 classifier 1 that was incorrect in classifier 2, and the number of correct samples for classifier 2
 329 that were incorrect in classifier 1, respectively. X^2 can be calculated using the following equation:

$$330 \quad X^2 = \frac{(f_{12} - f_{21})^2}{f_{12} + f_{21}} \quad (6)$$

331 A confidence level of 95% was used, which gives a critical value of 3.84, meaning that a null
 332 hypothesis can be rejected if the X^2 value exceeds 3.84. Figure 3 presents a full overview of this
 333 paper's methodological workflow.



334

335

336

Figure 3. Overview of the methodological structure of this study. Red represents radar processing, Green is optical and Blue is the SAGA Wetness Index.

337

3. Results

338

339

340

341

342

343

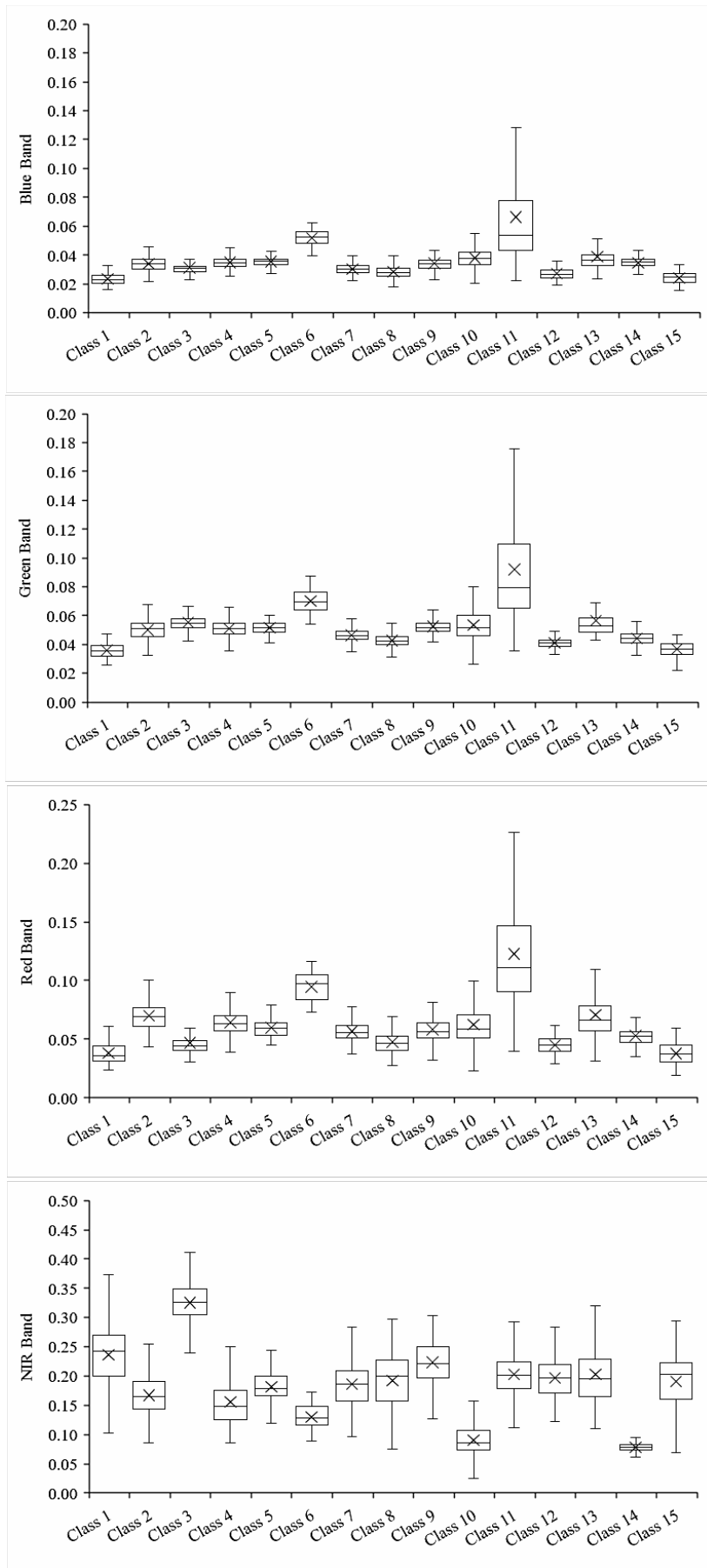
344

345

Prior to classification, the 45 sampled objects for each class were assessed using boxplots showing the upper and lower quartiles, median, mean and max/min values. The classes were plotted against every object and showed that not all features offered good delineation between all LULC and wetland and non-wetland classes. Figures 4 and 5 show the mean values for the optical features from Sentinel-2. The majority of classes for blue, green and red show very small interquartile ranges suggesting that the objects were of a suitable size and that there was little object-pixel heterogeneity. The mean blue and green show lower variability than the red band between classes, however, all showed high variability in the 'Sand/Soil' class. The mean NIR band

346 shows larger inter-class variance, except for *Wet Mudflat* which shows the lowest mean value
347 (0.08) with low variance. *Open Water*, *Low Vegetated Wetland*, *Dry Mudflat* and *Agricultural*
348 *Wetland (Low Productivity)* can all be moderately distinguished with NIR, however, *Woodland*,
349 *Thicket/Dense Bush*, and *High Vegetated Wetland* all show very similar variance with similar
350 mean values. The two optical derivatives (NDVI and MNDWI) offer valuable vegetation/non-
351 vegetation and water/non-water distinguishability respectively. NDVI shows low but similar
352 values for both mudflat classes, *Open Water* and *Sand/Soil*. It also offers clear separation
353 between highly and lowly productive agriculture for both wet and non-wetland classes. MNDWI
354 also separates both mudflat classes, *Open Water* and *Sand/Soil*, but with clear differentiation
355 between them, unlike NDVI. Finally, MNDWI does not offer the same separability as NDVI for
356 vegetation classes.

357

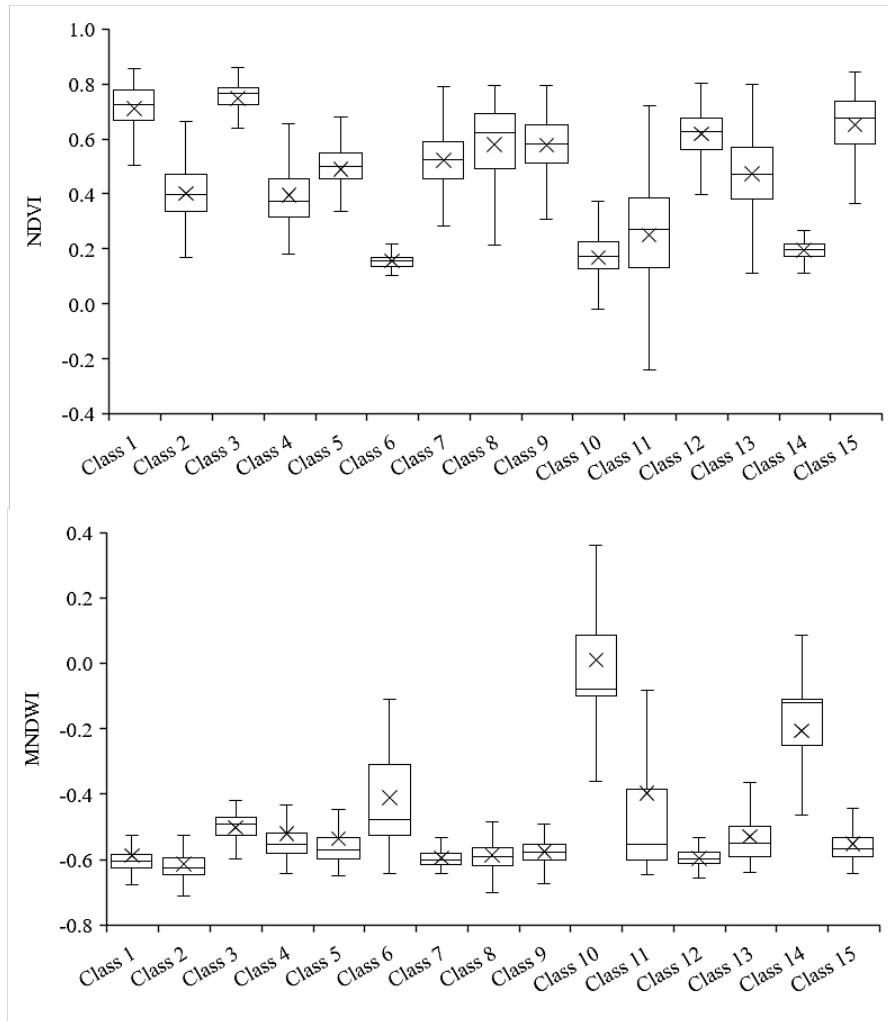


358

359

360

Figure 4. Box and whisker plots of the four 10 m Sentinel-2 bands showing mean, median, quartiles, maximum and minimum for each class (n=45).



362

363

364

Figure 5. Box and whisker plots for the two optically derived indices (NDVI and MNDWI), showing mean, median, quartiles, maximum and minimum for each class (n=45).

365

366

367

368

369

370

371

372

373

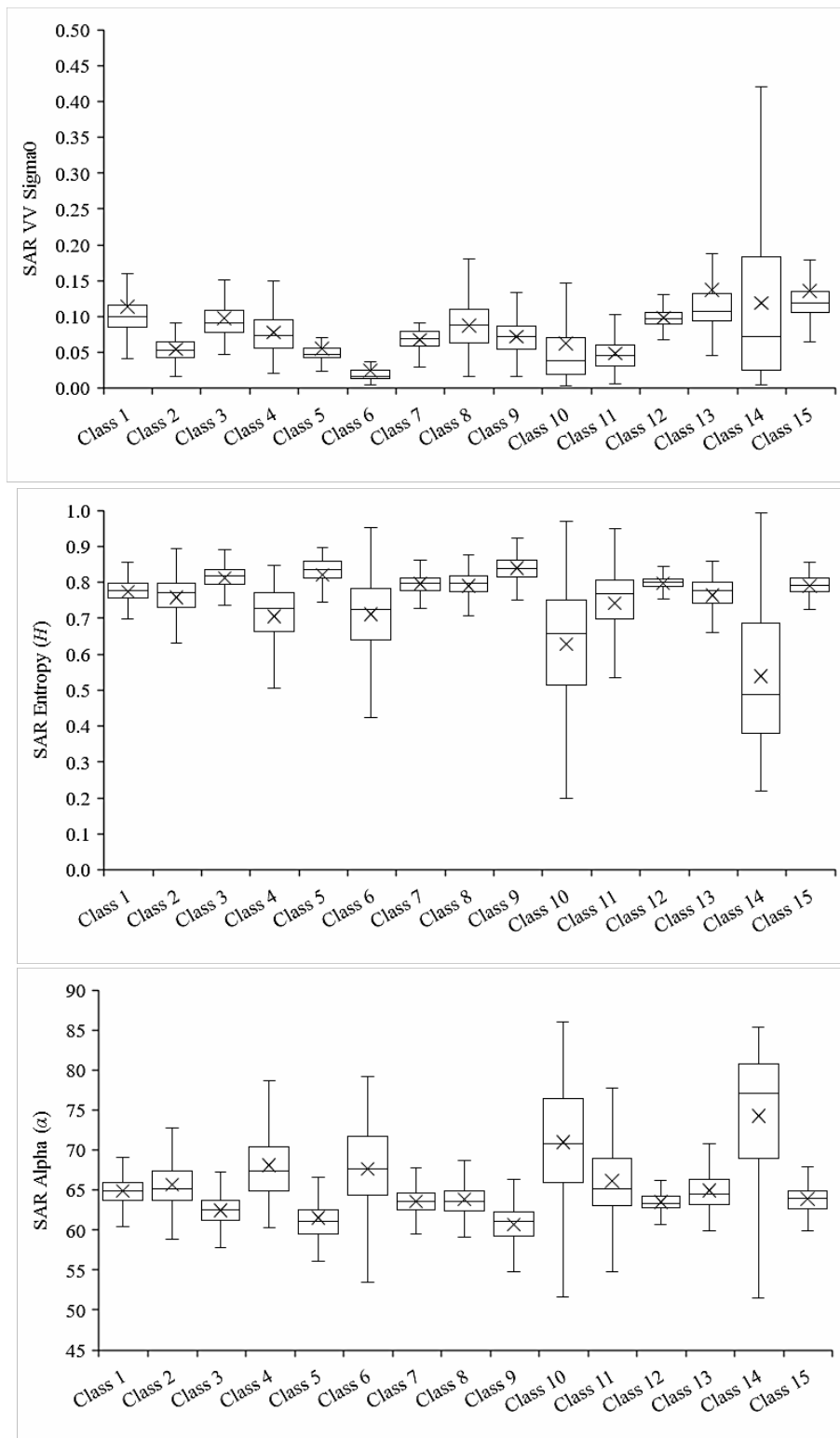
374

375

376

377

Figure 6 shows the mean object SAR values from the dual-polarized Sentinel-1. The VV σ^0 backscatter shows reasonable separation between classes, but some do overlap strongly. 'Agriculture (High Productivity)' and 'Thicket/Dense Bush' overlap; as well as 'Agriculture (Low Productivity)' and 'Sand/Soil'; and 'Agricultural Wetland (Low Productivity)', 'Grassland' and 'Low Vegetated Grassland'. The class 'Wet Mudflat' has a very large interquartile variance and min/max range (0.42), that contains all the other classes showing poor delineation. The plots also show boxplots for the $H-\alpha$ decomposition for entropy and alpha values. The wetland classes of 'Wet Mudflat', 'Open Water', 'Dry Mudflat' and 'Agricultural Wetland (Low Productivity)' all show high variance but are each distinguishable by their mean value. They fail to distinguish between 'Grassland', 'High Vegetated Wetland', 'Thicket/Dense Bush' and 'Woodland', although these classes do have very low variance.



378

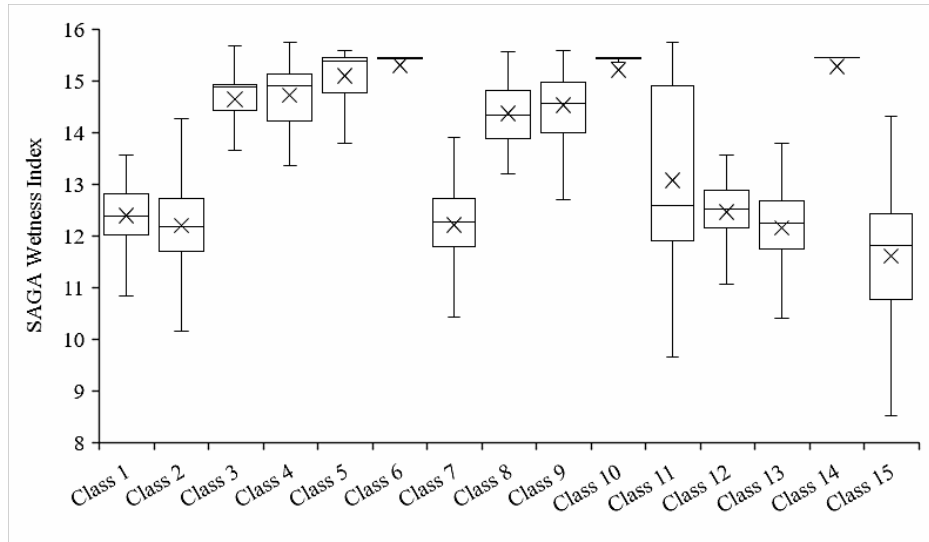
379 **Figure 6.** Box and whisker plots for the Sentinel-1 derived products (VV, entropy and alpha),
 380 showing mean, median, quartiles, maximum and minimum for each class (n=45).

381

382 The SWI separated wetland and non-wetland classes effectively (Figure 7). The mudflat and open
 383 water classes have extremely high SWI values with low interquartile variance and min/max
 384 range. Non-wetland classes overlapped largely with the exception of 'Woodland' that had the
 385 lowest SWI mean, but the largest min/max range. Of the wetland classes, the agricultural areas

386 showed strong overlap, as did the low and high vegetated areas. *'Aquatic Macrophyte'* could be
 387 distinguished reasonably well from the other classes. The class *'Sand/Soil'* had the largest
 388 variance merging across wetland and non-wetland classes. This class was not necessarily
 389 confined to either of these as it can be found in both.

390



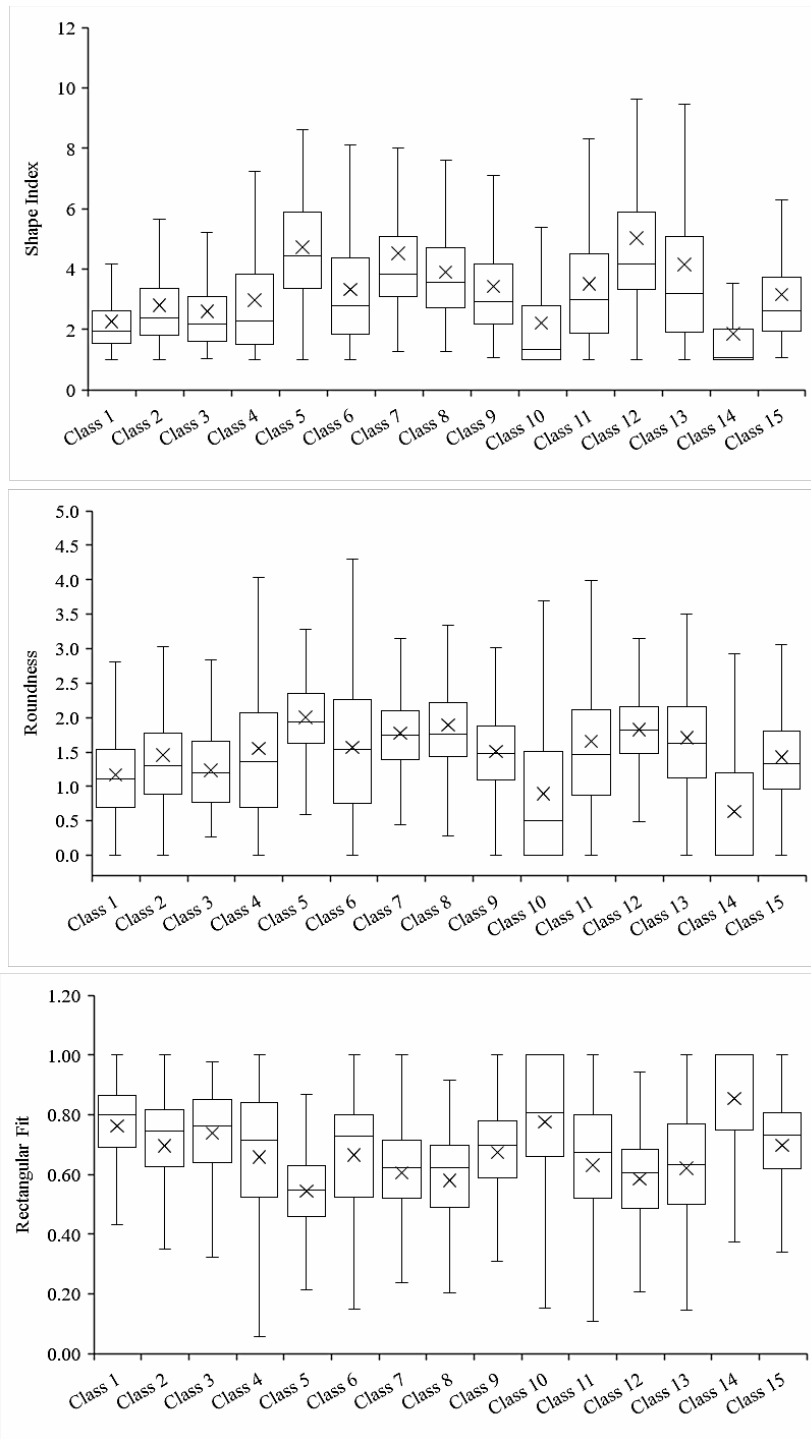
391

392 **Figure 7.** Box and whisker plot for the SAGA Wetness Index, showing mean, median, quartiles,
 393 maximum and minimum for each class (n=45).

394

395 The use of geometric features was also implemented in this study, showing the largest
 396 interquartile variance and min/max ranges (Figure 8). The shape index offered the best results of
 397 the three features. The four agricultural classes, *'Open Water'* and *'Wet Mudflat'* had the lowest
 398 values indicating smoother object edges, whereas *'Aquatic Macrophyte'*, *'Grassland'*,
 399 *'Thicket/Dense Bush'* and *'Urban'* all showed the largest values, suggesting rugged, broken edges.
 400 The roundness feature was useful in delineating *'Aquatic Macrophyte'* (high mean) and *'Open*
 401 *Water'* (low mean) objects. Rectangular fit showed the least promising results with very large
 402 overlaps in classes. Agricultural classes had high values, as well as, *'Open Water'* and *'Wet*
 403 *Mudflat'*.

404



405

406 **Figure 8.** Box and whisker plots for the geometric features derived from the image segmentation
 407 process, showing mean, median, quartiles, maximum and minimum for each class (n=45).

408

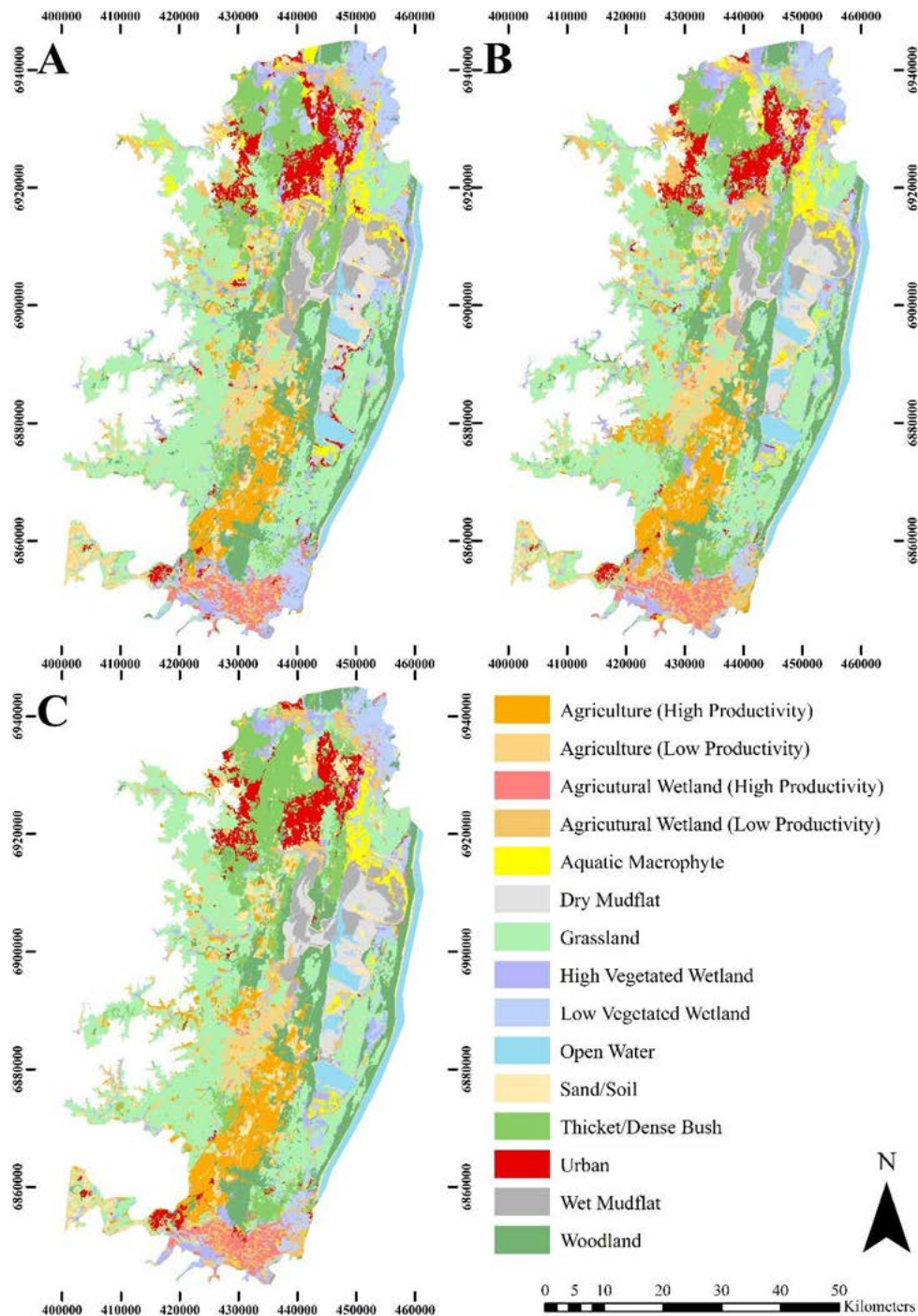
409 **3.1. Support Vector Machines**

410 The three classifications for SVMs can be seen in Figure 9, where (A) represents the *Op* classifier,
 411 (B) the *OpR* and (C) the *OpRS*. Through visual inspection (A) and (B) appear similar, but when
 412 compared to (C) it can be seen that '*Aquatic Macrophyte*' is much more dispersed, and wetland
 413 vegetation appears in patches amongst the grassland to the west of the study site. '*Urban*' is much
 414 less confined in the *Op* classifier with stretches appearing around the St. Lucia Lake fringe. The

415 southern region shows an area of agricultural wetland in all classifiers. The same is also occurring
416 to the northern region in the Mkhuze Swamp.

417 The accuracy assessments for the SVMs *Op*, *OpR* and *OpRS* can be seen in the left half of Table 3.
418 The highest overall accuracy came from the *OpRS* classifier at 79.8% ($K=0.68$), followed by the
419 *OpR* (75.8%, $K=0.7$) and *Op* (69.3%, $K=0.65$). For the highest performing classifier, 'Open Water'
420 had the greatest user accuracy (99.1%), closely followed by 'Dry Mudflat', 'Wet Mudflat' and
421 'Aquatic Macrophyte' (91.8%, 89.1% and 89.1%). The above mentioned also showed the top
422 producer accuracies at 97.3%, 84.9%, 90.7% and 94.2%, respectively. The lowest user accuracies
423 were seen in 'Grassland', 'Agriculture (High Productivity)' and 'Agriculture (Low Productivity)' with
424 62.7%, 63.6% and 67.3%, respectively. The lowest producer accuracies were seen in 'Agriculture
425 (High Productivity)', 'Sand/Soil' and 'Low Vegetated Wetland' with 66.7%, 71.5% and 73.2%,
426 respectively.

427



428

429 **Figure 9.** LULC classification maps produced by SVMs. (A) is optical only, (B) is optical and radar
 430 and (C) is optical, radar and SWI.

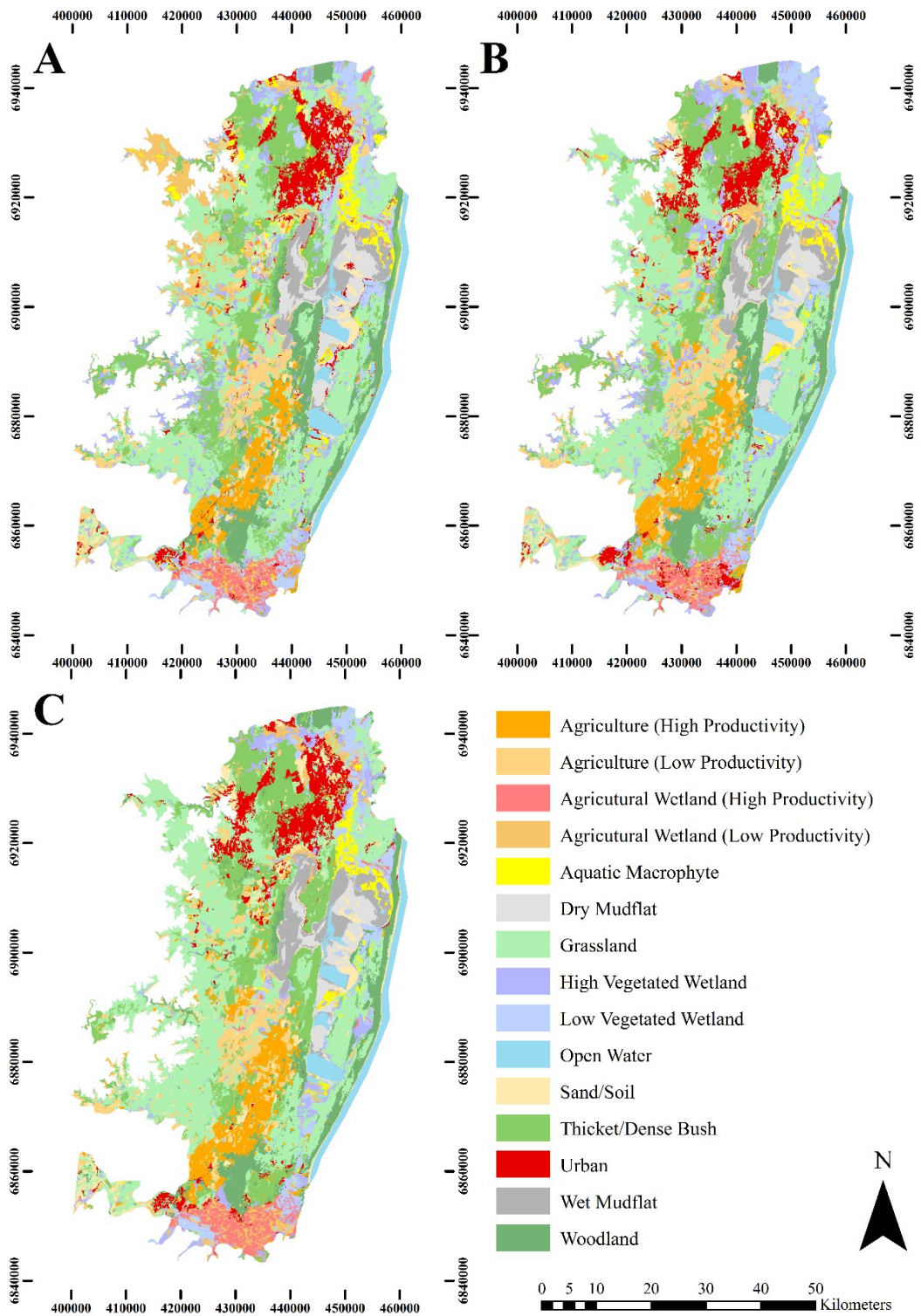
431

432 **3.2. Random Forests**

433 The three classifications for RFs can be seen in Figure 10, where (A) represents the *Op* classifier,
 434 (B) the *OpR* and (C) the *OpRS*. All three appear visually similar to the SVMs, with variations being
 435 hard to spot. The greatest differences can be seen in (A), where the northwest sparse urban area
 436 is redundant, approximately 10 km east of Ngwenya. (C) has less 'Woodland' but more
 437 'Grassland' and 'Thicket/Dense Bush'. In addition, RFs does not classify 'Urban' around the lake
 438 fringe to the same extent as SVMs.

439 The accuracy assessments for the RFs *Op*, *OpR* and *OpRS* can be seen in the right half of Table 3.
440 The highest overall accuracy came from the *OpRS* classifier at 83.3% ($K=0.72$), followed by the
441 *OpR* (78.2%, $K=0.7$) and *Op* (70.3%, $K=0.71$). For the highest performing classifier, 'Open Water'
442 had the greatest user accuracy (99.1%) closely followed by 'Dry Mudflat', 'Wet Mudflat' and
443 'Aquatic Macrophyte' (92.7%, 92.7% and 91.8%). The above mentioned also showed the top
444 producer accuracies at 97.3%, 87.9%, 91.1% and 94.4%, respectively. These are the same classes
445 as SVMs but with slightly higher values. The lowest user accuracies were seen in 'Agriculture (Low
446 Productivity)', 'Agriculture (High Productivity)' and 'Grassland' with 63.9%, 70.9% and 72.7%,
447 respectively. The lowest producer accuracies were seen in 'Agriculture (High Productivity)', 'High
448 Vegetated Wetland' and 'Woodland' with 71.6%, 72.4% and 77.0%, respectively.

449



450

451 **Figure 10.** LULC classification maps produced by RFs. (A) is optical only, (B) is optical and radar
 452 and (C) is optical, radar and SWI.

453

454

455

456

457 **Table 3.** Accuracy assessments for the three classifications. PA(%) is the Producer's accuracy and
 458 UA(%) is the User's accuracy. Class codes 1-15 are identified in Table 2 (n=1650).

Class code	Support Vector Machines						Random Forests					
	Optical Only		Optical and Radar Only		All		Optical Only		Optical and Radar Only		All	
	PA(%)	UA(%)	PA(%)	UA(%)	PA(%)	UA(%)	PA(%)	UA(%)	PA(%)	UA(%)	PA(%)	UA(%)
1	57.5	62.7	63.8	67.3	66.7	67.3	58.3	63.6	67.9	69.1	71.6	70.9
2	65.0	60.9	74.2	62.7	79.5	63.6	66.3	62.7	76.1	63.6	83.3	63.6
3	63.9	62.7	69.2	67.3	77.7	79.1	66.0	63.6	75.2	71.8	83.2	85.5
4	64.0	64.5	71.0	69.1	80.0	76.4	65.1	64.5	77.9	73.6	87.2	86.4
5	85.7	76.4	90.0	81.8	94.2	89.1	87.8	78.2	93.1	85.5	94.4	91.8
6	77.0	79.1	81.0	89.1	84.9	91.8	78.6	80.0	82.6	90.9	87.9	92.7
7	66.0	63.6	71.4	63.6	75.0	62.7	67.0	66.4	74.3	68.2	78.4	72.7
8	61.4	63.6	66.4	66.4	74.1	75.5	60.5	62.7	70.5	71.8	72.4	81.8
9	64.3	67.3	69.2	73.6	73.2	81.8	66.1	67.3	70.7	74.5	81.8	81.8
10	94.3	90.9	97.3	99.1	97.3	99.1	95.2	90.0	96.5	100.0	97.3	99.1
11	59.8	63.6	67.8	72.7	71.5	88.0	62.0	68.2	68.6	75.5	77.8	82.7
12	64.5	72.7	74.8	72.7	76.0	71.8	65.3	73.6	76.6	77.3	77.9	73.6
13	79.8	71.8	82.1	79.1	82.6	81.8	80.6	71.8	82.1	79.1	84.1	86.4
14	75.7	76.4	83.8	84.5	90.7	89.1	77.2	80.0	87.9	85.5	91.1	92.7
15	66.7	63.6	75.6	87.3	75.8	88.2	68.6	65.5	75.6	87.3	77.0	88.2

459

460

461 **3.3. Overall results**

462 The McNemar's test revealed that statistically in every case the *OpRS* out-outperformed *OpR* and *Op*
 463 and likewise for *OpR* against *Op*. The test also showed that in the majority of cases RFs
 464 outperformed SVMs at all levels. The exception being between RF_{Op} versus SVM_{Op} , and RF_{OpR}
 465 against SVM_{OpR} showing no statistical difference between them. Table 4 shows the adapted
 466 contingency matrix used to compare the six classifications. Bold values indicate a statistical
 467 difference between the two classifiers. A summary of the classifiers overall accuracy and Kappa
 468 values can be seen in Table 5. These are shown in rank order. Finally, Figure 11 shows the total
 469 wetland extent for the highest-ranking classification (RF_{OpRS}) which covers 932 km², equating to
 470 26.9% of the total study site area.

471

472

473

474

475

476
477

Table 4. The adapted contingency matrix used to compare all classifiers with one another. Numbers in bold indicate statistically better classifiers (95% confidence interval: 3.84).

		Support Vector Machines			Random Forests		
		Optical Only	Optical and Radar Only	All	Optical Only	Optical and Radar Only	All
Support Vector Machines	Optical Only						
	Optical and Radar Only	13.23					
	All	17.71	12.19				
Random Forests	Optical Only	0.94	4.26	16.43			
	Optical and Radar Only	17.99	2.05	9.11	11.12		
	All	21.36	8.89	10.42	17.45	9.91	

478
479
480

481 **Table 5.** Summary table of the overall accuracy for each classifier along with its relevant Kappa
482 value. They have been ranked in order of accuracy.

Data Combination	Classifier	Overall Accuracy (%)	Kappa Coefficient	Rank
All	RFs	83.3	0.72	1
All	SVMs	79.8	0.68	2
Optical and Radar	RFs	78.2	0.70	3
Optical and Radar	SVMs	75.8	0.70	4
Optical Only	RFs	70.3	0.71	5
Optical Only	SVMs	69.3	0.65	6

483
484
485
486



487

488 **Figure 11.** True color map with hill shade overlaid with a vector wetland file created by merging
 489 all wetland classes (*'Sand/Soil'* is not included).

490

491 **4. Discussion**

492 With the use of a multi-scale trial and error approach it was found that a heterogeneous wetland
 493 environment could be satisfactorily segmented to produce feature objects that represented the
 494 real world. When using a pixel based approach, images can have the so called 'salt and pepper
 495 effect', where real world features appear speckled due to the incorrect classification of pixels.
 496 OBIA moves around this issue, so long as the segmentation process is of a high standard. The trial
 497 and error technique that is so often used, provided a qualitative estimation for parameter
 498 selection with relatively accurate success. It was shown that diverse wetland landscapes are
 499 difficult to segment. A single segmentation level is often not adequate enough (Blaschke et al.,
 500 2008; Dronova, 2015), therefore a multi-level approach may be more effective, as was found in
 501 this study using a combination of multiresolution and spectral difference merge in a bottom-up
 502 approach. This has been effective in other LULC classifications (Im et al., 2008; Rampi et al., 2014)
 503 but has not been adequately implemented in wetland studies of this resolution. Other solutions
 504 could be the Estimation of Scale Parameter (ESP) tool (Drăguț et al., 2010; Drăguț et al., 2014) for
 505 use in eCognition, which automatically finds 'optimum' parameters for the entire scene using an

506 iterative object variance algorithm. This approach may save time for future studies and could
507 offer fully-automatic image segmentation.

508 The error matrices and McNemar's test show that when a synergistic use of Sentinel-1 and 2 is
509 implemented higher accuracies can be achieved than with optical only. This can then be improved
510 further with SWI. No statistical difference in accuracy could be seen between RF_{Op} versus SVM_{Op} ,
511 and RF_{OpR} against SVM_{OpR} . C-band dual-polarimetric SAR was deemed suitable in this study for
512 wetland LULC mapping. RFs variable importance showed that these were not preferred over
513 optical bands, but the boxplots in Figure 6 clearly show their capability. $VV \sigma^0$ backscatter showed
514 low inter-class variance but could not distinguish between '*Agriculture (High Productivity)*' and
515 '*Thicket/Dense Bush*', as well as other similar vegetation types. This has been attributed to the
516 wavelength of the SAR dataset which may struggle to penetrate the canopies, seeming to act as a
517 rough surface scatterer. Li et al. (2012) found the same issue with RADARSAT- 2 data on forested
518 and highly vegetated areas. An explanation for the large variance observed for '*Wet Mudflat*' may be
519 due to the interaction of C-band energy and in an M-shaped pattern of backscatter described by Lee
520 et al. (2011). This makes it extremely difficult to delineate this class with σ^0 backscatter alone.

521 The H-Alpha decomposition was derived from the SAR imagery and offered another dimension in
522 feature characteristics. The spread of H and α was very confined and the boxplots showed overlap
523 across classes. '*Grassland*', '*High Vegetated Wetland*', '*Thicket/Dense Bush*' and '*Woodland*' all
524 overlapped for their interquartile range but could be separated by the mean value. This is why the
525 mean of each feature was chosen, as it was felt that this offered the best chance of separation
526 amongst classes. '*High Vegetated Wetland*' did not show greater α values than '*Woodland*', which
527 would be expected for flooded vegetation. This could have been because of the wavelength of the
528 SAR like before, or possibly due to sensor incidence angle being too high (White et al., 2015) due
529 to the IW2 swath. Another reason may be because of the climatic conditions at the time of
530 capture. Drought in iSimangaliso Park means that the SAR is losing dimensionality.

531 Geometric features are one of the benefits of using OBIA, but overall results were rather
532 disappointing. The shape index offered the best input based on the RFs variable importance and
533 boxplot graphs. The agricultural classes all showed the lowest values due to their smooth edges,
534 proving more useful than rectangular fit, as Jiao et al. (2012) suggested. The heterogeneity of
535 many classes at this resolution is thought to explain the overall poor delineation of object features.
536 Finally, the SWI was sufficient in delineating the wetland from non-wetland classes, especially for
537 the '*Open Water*' and mudflat classes which is to be expected. These features occur where water is
538 most likely to drain, so although the mudflats have no water on them at the time, SWI can still
539 help locate these areas as Lang et al. (2012) described. '*Woodland*' was also well delineated by
540 SWI, showing the lowest values of any class. This is thought to be because the woodlands are
541 found in upland regions, usually on steeper slopes. As the study site is a reasonably low-lying
542 estuarine system, SWI is able to produce a more representative flow model across flat wetland
543 environments. The presented results contradict those of Huang et al. (2011), showing that a 30 m
544 DEM can statistically improve wetland classifications, although it does not offer much in regard to
545 non-wetland vegetated classes.

546 The parameter selection for both classifiers (SVMs and RFs) allowed for a fairer comparative
547 study, instead of using internal, classifier specific evaluation. The technique used here has been
548 successfully implemented in other LULC investigations (Petropoulos et al., 2012; Zhang and Xie,
549 2013; Sonobe et al., 2014). It was shown that RFs outperformed SVMs in all cases using error
550 matrices, and this was statistically proven with the McNemar's test. Differences observed with the
551 SVMs for the lowest user accuracies when compared to RFs could be explained by the sub-

552 sampling SVMs do at the hyperplane margins. Another thing to note is that the SVM took
553 particularly longer to compute than the RF classifier, which on larger, long-term studies, could
554 poses a problem.

555 Finally, this study presents a cost-effective technique to monitor the wetland with freely available
556 data at a good temporal resolution, due to the addition of Sentinel-1B and 2B. It was shown that a
557 reasonable accuracy can be achieved using the methods outlined here. eCognition is an expensive
558 software package but there is no reason why OBIA cannot be implemented in other freely
559 available programs, such as the Remote Sensing and GIS Software Library (RSGISLib) (Bunting et
560 al., 2014). However, the RSGISLib does not host the same segmentation algorithms, so further
561 research would be needed to find a suitable alternative.

562

563 **5. Conclusions**

564 This study, to our knowledge, is the first to evaluate the synergistic partnership of Sentinel-1 and
565 2 in the context of wetland studies using OBIA technique, offering an avenue for further research.
566 In addition, this study applied a multi-level OBIA for mapping wetland areas using Sentinel-1 and
567 2 data, and the results from its implementation were compared against two powerful machine
568 learning techniques. Findings of our study showed that RFs algorithm outperformed SVMs
569 marginally but consistently throughout. The synergistic approach showed an increase in terms of
570 the overall accuracies, which was even higher when the SWI was also included. The H-Alpha
571 decomposition was found to be effective at delineating certain LULC classes, particularly the low
572 vegetated and agricultural features. However, it is quite probable that the C-band wavelength was
573 too short to decompose accurate scattering mechanisms of highly vegetated regions where
574 canopies are dense. Geometric features did not appear to be aiding the classifiers much based on
575 boxplot interpretation and RFs variable importance, with some exception for the shape index.

576 Future work is required towards the investigation of the multi-temporal capability of this
577 approach and what it has to offer for the long-term study of wetlands under threat. In addition, it
578 would be interesting to conduct synergistic studies between Sentinel-2 and X- or L-band SAR EO
579 systems, to explore if the issue of dense canopy penetration experienced with the use of Sentinel-
580 1 can be overcome. Finally, further exploration of landscape derivatives from a range of sources
581 could be tested (e.g. LiDAR) with a range of flow algorithms, which could aid in finding a cost-
582 benefit between resolution and imagery cost.

583

584 **References**

585 Adam, E., Mutanga, O., Rugege, D., 2009. Multispectral and hyperspectral remote sensing for
586 identification and mapping of wetland vegetation: a review. *Wetlands Ecology and*
587 *Management* 18(3), 281-296.

588 Adams, J.B., Nondoda, S., Taylor, R.H., 2013. Macrophytes. In: Perissinotto, R., Stretch, D. D. and
589 Taylor, R. H. ed. *Ecology and Conservation of Estuarine Ecosystems: Lake St Lucia as a Global*
590 *Model*. Cambridge University Press, New York, pp.208–225.

591 Andersson, J., 2009. A GIS-based landscape analysis of dissolved organic carbon in boreal
592 headwater streams. MSc. Karlstad University.

- 593 Ardelean, F., Török-Oance, M., Urdea, P., Onaca, A., 2011. Application of object based image
594 analysis for glacial cirques detection. Case study: The Țarcu Mountains (Southern
595 Carpathians). *Forum Geographic* 10(1), 20-26.
- 596 Arenas, M., Pradenas, L., 2016. Implementation of an automatic satellite image georeferencing
597 adjustment method. *IEEE Latin America Transactions* 14(3), 1427- 1433.
- 598 Aschbacher, J., Milagro-Pérez, M., 2012. The European Earth monitoring (GMES) programme:
599 Status and perspectives. *Remote Sensing of Environment* 120, 3-8.
- 600 Aune-Lundberg, Linda, Geir-Harald Strand, Comparison of variance estimation methods for use
601 with two-dimensional systematic sampling of land use/land cover data, In *Environmental*
602 *Modelling & Software*, Volume 61, 2014, Pages 87-97,
603 <https://doi.org/10.1016/j.envsoft.2014.07.001>.
- 604 Bassa, Z., Bob, U., Szantoi, Z., Ismail, R., 2016. Land cover and land use mapping of the iSimangaliso
605 Wetland Park, South Africa: comparison of oblique and orthogonal random forest algorithms.
606 *Journal of Applied Remote Sensing* 10(1), p.015017.
- 607 Berger, M., Moreno, J., Johannessen, J., Levelt, P., Hanssen, R., 2012. ESA's sentinel missions in
608 support of Earth system science. *Remote Sensing of Environment* 120, 84-90.
- 609 Blaschke, T., Lang, S., Hay, G., 2008. *Object-based image analysis*. Springer, Berlin.
- 610 Breiman, L., 2001. Random Forests. *Machine Learning* 45(1), 5-32.
- 611 Bunting, P., Clewley, D., Lucas, R., Gillingham, S., 2014. The Remote Sensing and GIS Software
612 Library (RSGISLib). *Computers & Geosciences* 62, 216-226.
- 613 Cloude, S., 2007. The dual-polarization entropy/alpha decomposition: a pulsar case study. In:
614 *Proceedings of POLInSAR*. Frascati, pp. 1-6.
- 615 Cloude, S., Pottier, E., 1997. An entropy based classification scheme for land applications of
616 polarimetric SAR. *IEEE Transactions on Geoscience and Remote Sensing* 35(1), 68-78.
- 617 Congalton, R., 1991. A review of assessing the accuracy of classifications of remotely sensed data.
618 *Remote Sensing of Environment* 37(1), 35-46.
- 619 Coppola, B., 2015. iSimangaliso drought update - iSimangaliso Wetland Park.
620 [http://isimangaliso.com/newsflash/isimangaliso-
621 drought-update/](http://isimangaliso.com/newsflash/isimangaliso-drought-update/) (accessed 16 September 2016).
- 622 Cortes, C., Vapnik, V., 1995. Support-vector networks. *Machine Learning* 20(3), 273-297.
- 623 Davidson, N., 2014. How much wetland has the world lost? Long-term and recent trends in global
624 wetland area. *Marine and Freshwater Research* 65(10), 934.
- 625 de Leeuw, J., Jia, H., Yang, L., Liu, X., Schmidt, K., Skidmore, A., 2006. Comparing accuracy
626 assessments to infer superiority of image classification methods. *International Journal of*
627 *Remote Sensing* 27(1), 223-232.
- 628 d'Oleire-Oltmanns, S., Coenradie, B., Kleinschmit, B., 2011. An Object-Based Classification
629 Approach for Mapping Migrant Housing in the Mega-Urban Area of the Pearl River Delta
630 (China). *Remote Sensing* 3(12), 1710-1723.
- 631 Dorren, L., Maier, B., Seijmonsbergen, A., 2003. Improved Landsat-based forest mapping in steep
632 mountainous terrain using object-based classification. *Forest Ecology and Management*
633 183(1-3), 31-46.

- 634 Drăguț, L., Csillik, O., Eisank, C., Tiede, D., 2014. Automated parameterisation for multi-scale image
635 segmentation on multiple layers. *ISPRS Journal of Photogrammetry and Remote Sensing* 88,
636 119-127.
- 637 Drăguț, L., Tiede, D., Levick, S., 2010. ESP: a tool to estimate scale parameter for multiresolution
638 image segmentation of remotely sensed data. *International Journal of Geographical*
639 *Information Science* 24(6), 859-871.
- 640 Dronova, I., 2015. Object-Based Image Analysis in Wetland Research: A Review. *Remote Sensing*
641 7(5), 6380-6413.
- 642 Dronova, I., Gong, P., Wang, L., 2011. Object-based analysis and change detection of major wetland
643 cover types and their classification uncertainty during the low water period at Poyang Lake,
644 China. *Remote Sensing of Environment* 115(12), 3220-3236.
- 645 Du, Y., Zhang, Y., Ling, F., Wang, Q., Li, W., Li, X., 2016. Water Bodies' Mapping from Sentinel-2
646 Imagery with Modified Normalized Difference Water Index at 10-m Spatial Resolution
647 Produced by Sharpening the SWIR Band. *Remote Sensing* 8(4), 354.
- 648 Foody, G., 2004. Thematic Map Comparison. *Photogrammetric Engineering & Remote Sensing*
649 70(5), 627-633.
- 650 Forster, D., Kellenberger, T., Buehler, Y. and Lennartz, B., 2010. Mapping diversified peri-urban
651 agriculture – potential of object-based versus per-field land cover/land use classification.
652 *Geocarto International* 25(3), 171-186.
- 653 Frohn, R., Autrey, B., Lane, C., Reif, M. 2011. Segmentation and object-oriented classification of
654 wetlands in a karst Florida landscape using multi-season Landsat-7 ETM+ imagery.
655 *International Journal of Remote Sensing* 32(5), 1471-1489.
- 656 Furtado, L., Silva, T., Novo, E., 2016. Dual-season and full-polarimetric C band SAR assessment for
657 vegetation mapping in the Amazon várzea wetlands. *Remote Sensing of Environment* 174,
658 212-222.
- 659 Gauci, A., J. Abela, M. Austad, L.F. Cassar, K. Zarb Adami, A Machine Learning approach for
660 automatic land cover mapping from DSLR images over the Maltese Islands, In *Environmental*
661 *Modelling & Software*, Volume 99, 2018, Pages 1-10,
662 <https://doi.org/10.1016/j.envsoft.2017.09.014>.
- 663 Gedan, K., Kirwan, M., Wolanski, E., Barbier, E., Silliman, B., 2010. The present and future role of
664 coastal wetland vegetation in protecting shorelines: answering recent challenges to the
665 paradigm. *Climatic Change* 106(1), 7-29.
- 666 Gesler, W., 2005. Therapeutic landscapes: An evolving theme. *Health & Place* 11(4), 295-297.
- 667 Grenier, M., Labrecque, S., Garneau, M., Tremblay, A., 2008. Object-based classification of a SPOT-4
668 image for mapping wetlands in the context of greenhouse gases emissions: the case of the
669 Eastmain region, Québec, Canada. *Canadian Journal of Remote Sensing* 34(sup2), 398-413.
- 670 Guo, Y., Yu, X., Jiang, D., Wang, S., Jiang, X., 2012. Study on Forest Classification Based on Object
671 Oriented Techniques. *Geo-information Science* 14(4), 514-522.
- 672 Harken, J., Sugumaran, R., 2005. Classification of Iowa wetlands using an airborne hyperspectral
673 image: a comparison of the spectral angle mapper classifier and an object- oriented
674 approach. *Canadian Journal of Remote Sensing* 31(2), 167-174.

- 675 Huang, S., Young, C., Feng, M., Heidemann, K., Cushing, M., Mushet, D., Liu, S., 2011. Demonstration
676 of a conceptual model for using LiDAR to improve the estimation of floodwater mitigation
677 potential of Prairie Pothole Region wetlands. *Journal of Hydrology* 405(3-4), 417-426.
- 678 Im, J., Jensen, J., Tullis, J., 2008. Object-based change detection using correlation image analysis
679 and image segmentation. *International Journal of Remote Sensing* 29(2), 399-423.
- 680 Jiao, L., Liu, Y., Li, H., 2012. Characterizing land-use classes in remote sensing imagery by shape
681 metrics. *ISPRS Journal of Photogrammetry and Remote Sensing* 72, 46-55.
- 682 Jung, R., Adolph, W., Ehlers, M., Farke, H., 2015. A multi-sensor approach for detecting the
683 different land covers of tidal flats in the German Wadden Sea - A case study at Norderney.
684 *Remote Sensing of Environment* 170, 188-202.
- 685 Kavzoglu, T., Colkesen, I., 2009. A kernel functions analysis for support vector machines for land
686 cover classification. *International Journal of Applied Earth Observation and Geoinformation*
687 11(5), 352-359.
- 688 Kayranli, B., Scholz, M., Mustafa, A., Hedmark, Å., 2009. Carbon Storage and Fluxes within
689 Freshwater Wetlands: A Critical Review. *Wetlands* 30(1), 111-124.
- 690 Kennedy, R., Townsend, P., Gross, J., Cohen, W., Bolstad, P., Wang, Y., Adams, P., 2009. Remote
691 sensing change detection tools for natural resource managers: Understanding concepts and
692 tradeoffs in the design of landscape monitoring projects. *Remote Sensing of Environment*
693 113(7), 1382-1396.
- 694 Landis, J., Koch, G., 1977. The Measurement of Observer Agreement for Categorical Data.
695 *Biometrics* 33(1), 159.
- 696 Lang, M., McCarty, G., Oesterling, R., Yeo, I., 2012. Topographic Metrics for Improved Mapping of
697 Forested Wetlands. *Wetlands* 33(1), 141-155.
- 698 Lee, H., Chae, H., Cho, S., 2011. Radar Backscattering of Intertidal Mudflats Observed by Radarsat-
699 1 SAR Images and Ground-Based Scatterometer Experiments. *IEEE Transactions on*
700 *Geoscience and Remote Sensing* 49(5), 1701-1711.
- 701 Lee, J., 1981. Refined filtering of image noise using local statistics. *Computer Graphics and Image*
702 *Processing* 15(4), 380-389.
- 703 Li, G., Lu, D., Moran, E., Dutra, L., Batistella, M., 2012. A comparative analysis of ALOS PALSAR L-
704 band and RADARSAT-2 C-band data for land-cover classification in a tropical moist region.
705 *ISPRS Journal of Photogrammetry and Remote Sensing* 70, 26-38.
- 706 Loveline, E., 2015. Impacts of wetland degradation in Niger delta Nigeria and its significance in
707 flood control. *International Journal of Environment* 4(3), 177.
- 708 Macnae, W., 1963. Mangrove Swamps in South Africa. *The Journal of Ecology* 51(1), 1.
- 709 Malenovský, Z., Rott, H., Cihlar, J., Schaepman, M., García-Santos, G., Fernandes, R., Berger, M.,
710 2012. Sentinels for science: Potential of Sentinel-1, -2, and -3 missions for scientific
711 observations of ocean, cryosphere, and land. *Remote Sensing of Environment* 120, 91-101.
- 712 Mas, J.-F., Kolb, M., Paegelow, M., Camacho Olmedo, M.T., Houet, T. 2014. Inductive pattern-based
713 land use/cover change models: A comparison of four software packages. *Environmental*
714 *Modelling & Software* 51, 94-111, <https://doi.org/10.1016/j.envsoft.2013.09.010>.

- 715 Maxwell, A., Warner, T., Strager, M., 2016. Predicting Palustrine Wetland Probability Using
716 Random Forest Machine Learning and Digital Elevation Data-Derived Terrain Variables.
717 Photogrammetric Engineering & Remote Sensing 82(6), 437-447.
- 718 McFeeters, S., 1996. The use of the Normalized Difference Water Index (NDWI) in the delineation
719 of open water features. *International Journal of Remote Sensing* 17(7), 1425-1432.
- 720 Mellor, A., Haywood, A., Stone, C., Jones, S., 2013. The Performance of Random Forests in an
721 Operational Setting for Large Area Sclerophyll Forest Classification. *Remote Sensing* 5(6),
722 2838-2856.
- 723 Mui, A., He, Y., Weng, Q., 2015. An object-based approach to delineate wetlands across landscapes
724 of varied disturbance with high spatial resolution satellite imagery. *ISPRS Journal of*
725 *Photogrammetry and Remote Sensing* 109, 30-46.
- 726 Murayama, Y., 2012. *Progress in geospatial analysis*. Springer, Tokyo.
- 727 Murray-Rust, D., Robinson, D.T., Guillem, E., Karali, E., Rounsevell, M. 2014. An open framework
728 for agent based modelling of agricultural land use change. *Environmental Modelling &*
729 *Software* 61, 19-38, <https://doi.org/10.1016/j.envsoft.2014.06.027>.
- 730 Niculescu, S., Lardeux, C., Hanganu, J., 2017. Synergy between Sentinel-1 radar time series and
731 Sentinel-2 optical for the mapping of restored areas in Danube delta. In 28th International
732 Cartographic Conference.
- 733 Paneque-Gálvez, J., Mas, J., Moré, G., Cristóbal, J., Orta-Martínez, M., Luz, A., Guèze, M., Macía, M.,
734 Reyes-García, V., 2013. Enhanced land use/cover classification of heterogeneous tropical
735 landscapes using support vector machines and textural homogeneity. *International Journal*
736 *of Applied Earth Observation and Geoinformation* 23, 372-383.
- 737 Petropoulos, G., Kalaitzidis, C., Prasad Vadrevu, K., 2012. Support vector machines and object-
738 based classification for obtaining land-use/cover cartography from Hyperion hyperspectral
739 imagery. *Computers & Geosciences* 41, 99-107.
- 740 Petropoulos, G.P., Partsinevelos, P., Mitraka, Z., 2013. Change detection of surface mining activity
741 and reclamation based on a machine learning approach of multi-temporal Landsat TM
742 imagery. *Geocarto International* 28, 323-342, doi: 10.1080/10106049.2012.706648
- 743 Rampi, L., Knight, J., Pelletier, K., 2014. Wetland Mapping in the Upper Midwest United States.
744 *Photogrammetric Engineering & Remote Sensing* 80(5), 439-448.
- 745 Rastner, P., Bolch, T., Notarnicola, C., Paul, F., 2014. A Comparison of Pixel- and Object-Based
746 Glacier Classification with Optical Satellite Images. *IEEE Journal of Selected Topics in Applied*
747 *Earth Observations and Remote Sensing* 7(3), 853-862.
- 748 Rippon, S., 2009. 'Uncommonly rich and fertile' or 'not very salubrious'? The Perception and Value
749 of Wetland Landscapes. *Landscapes* 10(1), 39-60.
- 750 Robson, B., Nuth, C., Dahl, S., Hölbling, D., Strozzi, T., Nielsen, P., 2015. Automated classification of
751 debris-covered glaciers combining optical, SAR and topographic data in an object-based
752 environment. *Remote Sensing of Environment* 170, 372-387.
- 753 Rogan, J., Franklin, J., Stow, D., Miller, J., Woodcock, C., Roberts, D., 2008. Mapping land-cover
754 modifications over large areas: A comparison of machine learning algorithms. *Remote*
755 *Sensing of Environment* 112(5), 2272-2283.

- 756 Scott, D., Petropoulos, G.P., Moxley, J., Malcolm, H., 2014. Quantifying the physical composition of
757 urban morphology throughout Wales based on the time series (1989-2011) analysis of
758 Landsat TM/ETM+ images and supporting GIS data. *Remote Sensing* 6, 11731-11752,
759 doi:10.3390/rs61211731
- 760 Sesnie, S., Finegan, B., Gessler, P., Thessler, S., Ramos Bendana, Z., Smith, A., 2010. The
761 multispectral separability of Costa Rican rainforest types with support vector machines and
762 Random Forest decision trees. *International Journal of Remote Sensing* 31(11), 2885-2909.
- 763 Shang, X., Chisholm, L., 2014. Classification of Australian native forest species using hyperspectral
764 remote sensing and machine-learning classification algorithms. *IEEE Journal of Selected
765 Topics in Applied Earth Observations and Remote Sensing* 7(6), 2481-2489.
- 766 Shitole, S., De, S., Rao, Y., Krishna Mohan, B., Das, A., 2015. Selection of Suitable Window Size for
767 Speckle Reduction and Deblurring using SOFM in Polarimetric SAR Images. *Journal of the
768 Indian Society of Remote Sensing* 43(4), 739-750.
- 769 Sonobe, R., Tani, H., Wang, X., Kobayashi, N., Shimamura, H., 2014. Parameter tuning in the
770 support vector machine and random forest and their performances in cross- and same-year
771 crop classification using TerraSAR-X. *International Journal of Remote Sensing* 35(23), 7898-
772 7909.
- 773 Szantoi, Z., Escobedo, F., Abd-Elrahman, A., Smith, S., Pearlstine, L., 2013. Analyzing fine-scale
774 wetland composition using high resolution imagery and texture features. *International
775 Journal of Applied Earth Observation and Geoinformation* 23, 204-212.
- 776 Taşdemir, K., Milenov, P., Tapsall, B., 2012. A hybrid method combining SOM- based clustering and
777 object-based analysis for identifying land in good agricultural condition. *Computers and
778 Electronics in Agriculture* 83, 92-101.
- 779 Thompson, M., 1996. A standard land-cover classification scheme for remote-sensing applications
780 in South Africa. *South African Journal of Science* 92(1), 34-42.
- 781 Wang, L., Sousa, W., Gong, P., 2004. Integration of object-based and pixel-based classification for
782 mapping mangroves with IKONOS imagery. *International Journal of Remote Sensing* 25(24),
783 5655-5668.
- 784 Wang, P., Ma, Q., Wang, J., Hong, W., Li, Y., Chen, Z., 2013. An improved SAR radiometric terrain
785 correction method and its application in polarimetric SAR terrain effect reduction. *Progress
786 In Electromagnetics Research B* 54, 107-128.
- 787 White, L., Brisco, B., Daboor, M., Schmitt, A., Pratt, A., 2015. A collection of SAR methodologies for
788 monitoring wetlands. *Remote Sensing* 7(6), 7615-7645.
- 789 Whitfield, A., Taylor, R., 2009. A review of the importance of freshwater inflow to the future
790 conservation of Lake St Lucia. *Aquatic Conservation: Marine and Freshwater Ecosystems*
791 19(7), 838-848.
- 792 Xie, L., Zhang, H., Wang, C., Shan, Z., 2015. Similarity analysis of entropy/alpha decomposition
793 between HH/VV dual- and quad-polarization SAR data. *Remote Sensing Letters* 6(3), 228-
794 237.
- 795 Xu, Guang, Xuan Zhu, Dongjie Fu, Jinwei Dong, Xiangming Xiao, Automatic land cover classification
796 of geo-tagged field photos by deep learning, In *Environmental Modelling & Software*, Volume
797 91, 2017, Pages 127-134, <https://doi.org/10.1016/j.envsoft.2017.02.004>.

- 798 Xu, H., 2006. Modification of normalised difference water index (NDWI) to enhance open water
799 features in remotely sensed imagery. *International Journal of Remote Sensing* 27(14), 3025-
800 3033.
- 801 Zhang, C., Xie, Z., 2013. Object-based vegetation mapping in the Kissimmee river watershed using
802 HyMap data and machine learning techniques. *Wetlands* 33(2), 233-244.
- 803